Article

Not peer-reviewed version

The Impact of Aluminum Doping on the Performance of MgV_2O_4 Spinel Cathodes for High-Rate Zinc-Ion Energy Storage

He Lin *, Zhiwen Wang , Yu Zhang

Posted Date: 31 March 2025

doi: 10.20944/preprints202503.2266.v1

Keywords: zinc-ion batteries; cathode materials; vanadium oxide; aluminum doping

Article

The Impact of Aluminum Doping on the Performance of MgV_2O_4 Spinel Cathodes for High-Rate Zinc-Ion Energy Storage

He Lin *, Zhiwen Wang and Yu Zhang

A State Key Laboratory of Chemistry and Utilization of Carbon Based Energy Resources, School of Chemistry, Xinjiang University, Urumqi 830017, China; lefpullpelera@mail.com (Z.W.); cnuo017@gmail.com (Y.Z.)

* Correspondence: helin@xju.edu.cn; Tel.: +86-189-6386-3902

Abstract: This study explores the development of aluminum doped MgV_2O_4 spinel cathodes for aqueous zinc-ion batteries (AZIBs), aiming to overcome the challenges of poor ion diffusion and structural instability. Al^{3+} ions were pre-inserted into the spinel structure using a sol-gel method, enhancing the material's structural stability and electrical conductivity. The Al^{3+} doping mitigates the electrostatic interactions between Zn^{2+} ions and the cathode, improving ion diffusion and facilitating efficient charge/discharge processes. The resulting Al-MgV_2O_4 cathode demonstrates excellent electrochemical performance, retaining a capacity of 254.3 mAh g^{-1} at an ultra-high current density of 10 A g^{-1} after 1000 cycles, with a capacity retention of 93.6%. At an ultra-high current density of 20 A g^{-1}, the material retains 186.8 mAh g^{-1} after 2000 cycles, with a capacity retention of 90.2%, making it a promising candidate for high-rate energy storage applications.

Keywords: zinc-ion batteries; cathode materials; vanadium oxide; aluminum doping

1. Introduction

The escalating global demand for energy, coupled with the growing environmental pollution, poses a significant challenge, exacerbating both the energy crisis and environmental degradation [1]. In response, the pursuit of carbon neutrality has emerged as a key priority in global agendas. The increasing concentration of carbon dioxide is a major catalyst for the rapid expansion of renewable energy sources, such as solar and wind power [2,3]. However, the efficient integration of these renewable sources into the energy grid is contingent upon their effective transportation and storage [4]. In this context, electrochemical energy storage systems, particularly batteries, are regarded as critical for the storage of renewable energy [5]. Lithium-ion batteries (LIBs), which have long been the dominant technology for energy storage, are widely utilized in portable electronics, including smartphones and laptops, as well as in large-scale applications such as electric vehicles [6,7]. The high energy density and extended cycle life of LIBs have contributed to their attractiveness. However, despite these advantages, the long-term sustainability of LIBs is constrained by several challenges, including the finite global reserves of lithium, safety concerns, and high production costs [8,9]. These limitations raise concerns about the viability of LIBs for widespread adoption in the coming decades.

In light of the limitations of LIBs, there is an increasing focus on alternative battery technologies that utilize more abundant and environmentally benign materials, such as sodium (Na^+) [10], potassium (K^+) [11], and multivalent ions, including magnesium (Mg^{2+}) [12], zinc (Zn^{2+}) [13]. Among these, aqueous zinc-ion batteries (AZIBs) have attracted significant attention due to their promising electrochemical characteristics. Zinc is not only abundant and cost-effective but also amenable to direct use as an anode material, which substantially reduces manufacturing costs. Additionally, zinc exhibits a relatively high theoretical capacity of 820 mAh g^{-1} and a redox potential of −0.763 V versus the standard hydrogen electrode (SHE), making it a compelling alternative for energy storage [14–18]. AZIBs utilize slightly acidic or near-neutral aqueous electrolytes (pH 3.6–6.0), which enhance

 doi:10.20944/preprints202503.2266.v1

cycle safety and contribute to improved reversible capacity. The high ionic conductivity of aqueous electrolytes (1 S cm^{-1}) in comparison to organic electrolytes (1 to 10 mS cm^{-1}) facilitates faster ion migration, potentially enhancing the overall charging and discharging performance. As a result, AZIBs offer a promising, environmentally friendly, and sustainable alternative to LIBs for large-scale energy storage. However, despite their advantages, the development of suitable cathode materials for AZIBs remains a significant challenge. Issues such as cathode dissolution, structural instability during charge and discharge cycles, inefficient zinc ion intercalation and deintercalation, and slow reaction kinetics persist, highlighting the urgent need for the development of advanced cathode materials that demonstrate high specific capacity, improved rate performance, and enhanced cycle stability [19–21].

Recent research on cathode materials for AZIBs has primarily focused on manganese-based compounds [22–24], vanadium-based compounds [25–28], Prussian blue analogs (PBAs) [29–31], and organic materials [32,33]. Among these, vanadium-based materials, particularly vanadium oxides, have garnered significant interest due to their ability to exhibit multiple valence states (+5, +4, +3, +2) and a variety of crystal structures, including layered, quasi-layered, and tunnel configurations [34–37]. These structural variations present opportunities for the design of novel electrode materials with distinct and tunable electrochemical properties [38,39]. Despite their promising characteristics, vanadium-based cathode materials are hindered by several challenges, including poor electrical conductivity, low ion diffusion coefficients, and structural instability during charge and discharge cycles.

One promising approach to overcoming these challenges is the use of spinel-type vanadium oxide structures. Spinel materials, known for their extensive internal three-dimensional space, are capable of accommodating ion insertion and have been widely utilized in various battery systems, including LIBs [40–42]. In the context of AZIBs, spinel materials such as $ZnMn_2O_4$ [43], $ZnCo_2O_4$ [44], and $MgMn_2O_4$ [45] have been explored; however, vanadium-based spinel cathode materials have been less extensively investigated. Recent studies on MgV_2O_4 (MgVO), a vanadium-based spinel material, have demonstrated that electrochemical cycling can enhance the vanadium valence state, resulting in a notable reversible capacity of 128.9 mAh g^{-1} after 500 cycles at a current density of 4.0 A g^{-1} [46]. Nevertheless, the diffusion of Zn^{2+} within the spinel matrix is constrained by strong electrostatic interactions between the cathode host and the Zn^{2+} ions, which limits the ion diffusion kinetics.

Doping vanadium oxide with metal cations such as K^+, Mg^{2+}, has been demonstrated to enhance the structural stability, ion diffusion kinetics, and electronic conductivity of the material [47,48]. Aluminum (Al) is one of the most abundant metals in the Earth's crust and offers several advantages over transition metals, including low cost and low toxicity. The Al^{3+} ion forms strong Al–O bonds with oxygen atoms, with bond energies significantly higher than those of Na–O, K–O, and other alkaline metal–O bonds. These properties make aluminum an attractive candidate for improving the performance of vanadium-based cathodes [49].

Motivated by these considerations, we employed a sol-gel method to pre-insert Al^{3+} ions into the spinel MgVO structure, thereby enhancing its structural stability and improving its conductivity. The Al^{3+} ions form Al–O bonds, which mitigate the electrostatic interactions between Zn^{2+} ions and the host material, facilitating the intercalation and deintercalation of Zn^{2+} ions. The resulting Al-doped MgVO cathode material (Al-MgVO) exhibits improved ion diffusion, enhanced conductivity, and excellent electrochemical performance. At an ultra-high current density of 10 A g^{-1}, the material retains a capacity of 254.3 mAh g^{-1} after 1000 cycles, with a capacity retention of 93.6%. Additionally, at 20 A g^{-1}, the material maintains a capacity of 186.8 mAh g^{-1} after 2000 cycles, with a capacity retention of 90.2%, demonstrating its potential for high-rate applications.

 doi:10.20944/preprints202503.2266.v1

2. Results and Discussion

2.1. Morphological Characterization

The Al-MgVO composite was synthesized via the sol-gel method. To determine its elemental composition, Inductively Coupled Plasma (ICP) analysis was conducted. The results, presented in Table 1, provide a detailed insight into the material's composition. The ICP analysis reveals the chemical formula of the synthesized Al-MgVO to be $Al_{0.26}Mg_{1.23}V_2O_4$, confirming the successful incorporation of Al^{3+} into the MgVO framework.

Table 1. ICP measurements: ratio of Al, Mg, and V elements in Al-MgVO

Sample	Magnesium (mg/kg)×10⁴	Vanadium (mg/kg)×10⁴	Aluminium (mg/kg)×10⁴	Mg/V/Al
Al-MgVO	10.98	37.24	2.58	1.23/2/0.26

The X-ray diffraction (XRD) analysis of MgVO and Al-MgVO was conducted to characterize the phase and purity of both materials, with the results presented in Figure 1. As depicted in Figure 1a, the diffraction peaks of the Al-MgVO sample, doped with Al, are consistent with those of the undoped MgVO. All peaks correspond to the MgV_2O_4 standard (JCPDS No. 89-7410), and no additional peaks indicative of new phases were observed. This suggests that the Al doping did not induce the formation of any new crystalline phases, and the crystal structure of Al-MgVO remains largely unchanged in comparison to the original MgVO.

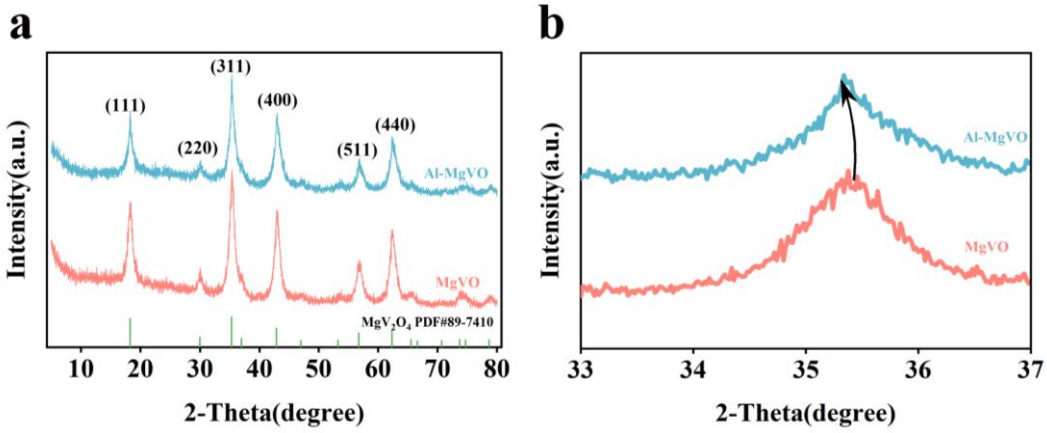

Figure 1. (**a**) XRD spectra of MgVO and Al-MgVO; (**b**) Enlarged view of the diffraction peak (311).

A slight variation is evident in Figure 1b, where the (311) diffraction peak of Al-MgVO shows a minor shift relative to that of MgVO. Specifically, the peak position shifts from 35.6° for MgVO to 35.3° for Al-MgVO. This shift implies an expansion of the interplanar spacing of the (311) crystal plane in Al-MgVO, which can be attributed to the substitution of Mg^{2+} with Al^{3+} ions in the MgVO lattice.

X-ray photoelectron spectroscopy (XPS) was employed to analyze the chemical composition and oxidation states of elements in the Al-MgVO sample. As shown in Figure 2a, the full XPS spectrum reveals the presence of Al, Mg, V, and O elements. The high-resolution V 2p spectrum in Figure 2b exhibits six peaks corresponding to the V $2p_{3/2}$ and V $2p^{1/2}$ binding energies at 516.5 eV, 522.1 eV, 516.9 eV, 523.6 eV, 517.8 eV, and 525.1 eV. These peaks are attributed to the V^{3+}, V^{4+}, and V^{5+} oxidation states. The peak at 516.9 eV, which is assigned to V^{4+}, is the dominant oxidation state in the Al-doped MgVO sample. This suggests that Al doping stabilizes V^{4+} in the MgVO structure, while the presence of V^{3s+} and V^{5+} indicates a mixed-valence state of vanadium within the system. The Mg 1s spectrum, shown in Figure 2c, exhibits a peak at 1304.18 eV, consistent with the Mg 1s binding energy. Additionally,

 doi:10.20944/preprints202503.2266.v1

Figure 2d presents the Al 2p spectrum, where a peak at 71.2 eV corresponds to Al 2p, while an additional peak at 74.2 eV further confirms the successful incorporation of Al into the MgVO matrix. This additional peak suggests the formation of Al–O bonds, implying that Al not only substitutes into the MgVO structure but also participate in bonding with oxygen, thereby contributing to the stability of the Al-doped material.

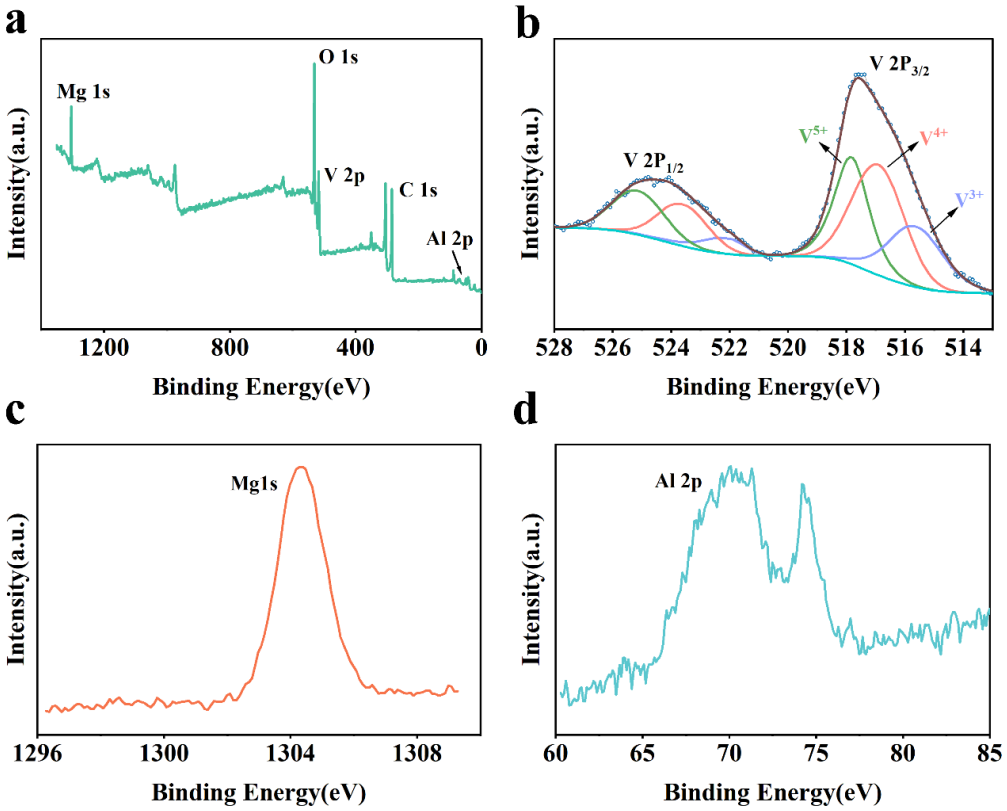

Figure 2. (**a**) XPS full spectrum of Al-MgVO; (**b**) XPS high-resolution spectrum of V 2p; (**c**) XPS spectrum of Mg 1s; (**d**) XPS spectrum of Al 2p.

The surface morphology of the Al-MgVO sample was characterized using scanning electron microscopy (SEM), and the results are presented in Figure 3. Figures 3a and 3b show the SEM images of Al-MgVO at different magnifications. The Al-MgVO sample exhibits a dispersed surface morphology composed of irregular block-like structures and microspheres with inconsistent sizes ranging from 1 to 3 μm. Upon further magnification in Figure 3b, nanoscale microspherical structures can be observed on the surface of the block-like particles. This nanoscale feature is likely a result of aggregation during the synthesis process, leading to the formation of both dispersed spherical and irregular block-like structures at the micron scale. The presence of nanoscale microspheres on the block surface is beneficial for increasing the contact area between the cathode material and the electrolyte, which can enhance the electrical conductivity and overall electrochemical performance of the material. Additionally, Energy-dispersive spectroscopy (EDS) mapping shown in Figure 3c clearly illustrates the homogeneous distribution of Al, Mg, V, and O elements within the Al-MgVO structure, further confirming the successful incorporation of aluminum into the matrix and its uniform distribution throughout the material.

 doi:10.20944/preprints202503.2266.v1

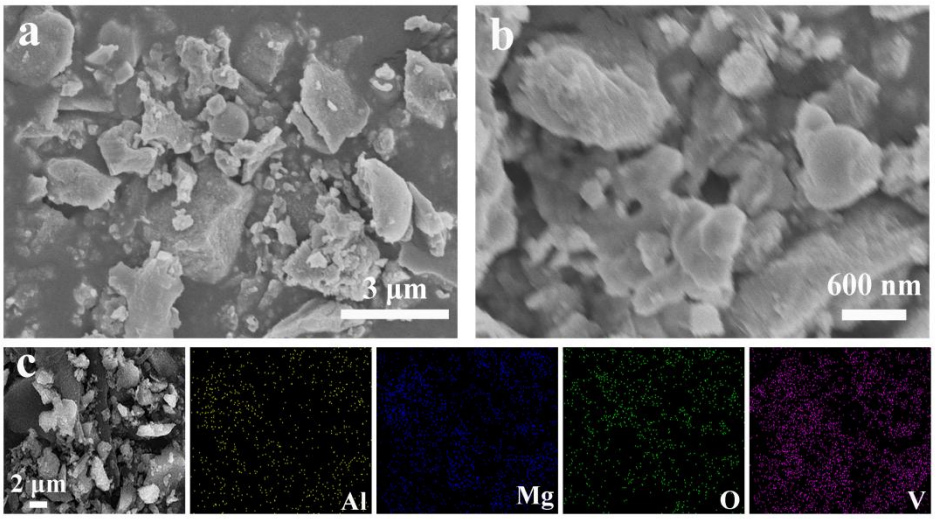

Figure 3. (**a**–**b**) SEM patterns of Al-MgVO; (**c**) EDS mapping of Al-MgVO.

2.2. Electrochemical Properties Characterization

The zinc-ion storage performance of the Al-MgVO material was investigated by assembling a CR2032 coin cell with Al-MgVO as the cathode, Zn as the anode, 3M $Zn(CF_3SO_3)_2$ aqueous electrolyte, and a glass fiber separator. The galvanostatic charge-discharge (GCD) profiles (Figure 4a) reveal a stable plateau around 1.5 V during the first charge, which disappears in subsequent charging cycles. This plateau suggests a reversible redox process associated with the insertion and extraction of zinc ions within the Al-MgVO structure. The initial charge capacity of the battery is 273.9 mAh g^{-1}, which is significantly higher than its initial discharge capacity, indicating the activation of the material and the formation of a stable electrochemical interface in the first cycle. During subsequent cycles, the charge and discharge curves gradually converge, demonstrating excellent reversibility and minimal capacity fading. This behavior suggests the stable cycling performance of Al-MgVO as a cathode material for zinc-ion batteries.

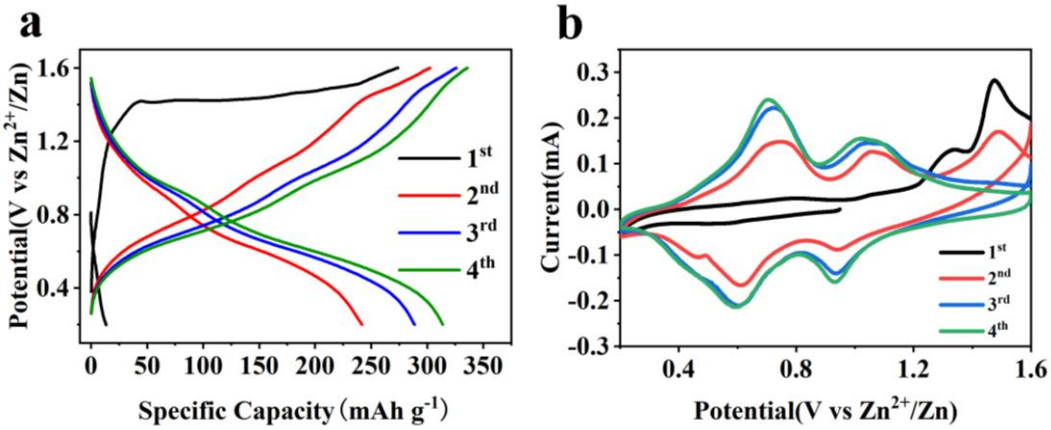

Figure 4. (**a**) Charge and discharge curve of the first four rounds of Al-MgVO; (**b**) the CV cycle curve corresponding to (**a**).

Complementary to the GCD analysis, cyclic voltammetry (CV) curves (Figure 4b) provide further insights into the electrochemical kinetics and redox behavior of Al-MgVO. In the first cycle, a pronounced oxidation peak appears around 1.5 V, consistent with the charge plateau observed in the GCD curve. This peak diminishes significantly in the second cycle, and eventually disappears in the following cycles, indicating the stabilization of the electrochemical processes and the completion of any initial electrochemical activation. The disappearance of the oxidation peak in subsequent cycles

 doi:10.20944/preprints202503.2266.v1

further corroborates the reversible nature of the zinc-ion intercalation and deintercalation within the Al-MgVO structure, aligning with the trends observed in the GCD profiles.

To further investigate the electrochemical performance of the Al-MgVO sample, the cycling stability and rate capability were evaluated. Figure 5a presents the cycling performance of MgVO and Al-MgVO as the cathode at a current density of 0.1 A g^{-1}. The initial discharge capacity of the Al-MgVO system was 13.5 mAh g^{-1}. However, the material subsequently achieved a charge capacity of 338.5 mAh g^{-1}, which further increased to a final capacity of 341.6 mAh g^{-1} after several cycles, with a Coulombic efficiency of 100% after 7 cycles. This indicates a rapid activation process followed by stable cycling behavior. After 53 charge-discharge cycles, the capacity was maintained at 315.1 mAh g^{-1}, resulting in a capacity retention of 92.2%. During the first seven cycles, the capacity increased, reaching a peak before stabilizing, which can be attributed to the deep activation of the electrode material and the gradual reduction of impedance, a trend that is consistent with the subsequent electrochemical impedance spectroscopy (EIS) results. In comparison to the MgVO electrode, which required a longer activation period, the initial specific capacities of MgVO and Al-MgVO were similar over the first 25 cycles. However, after 25 cycles, the capacity of MgVO began to degrade significantly, while Al-MgVO maintained a stable capacity without any noticeable fading. This suggests that the incorporation of Al^{3+} into the MgVO crystal structure does not lead to significant occupancy of Zn^{2+} sites, thus preserving the structural integrity and electrochemical performance of Al-MgVO.

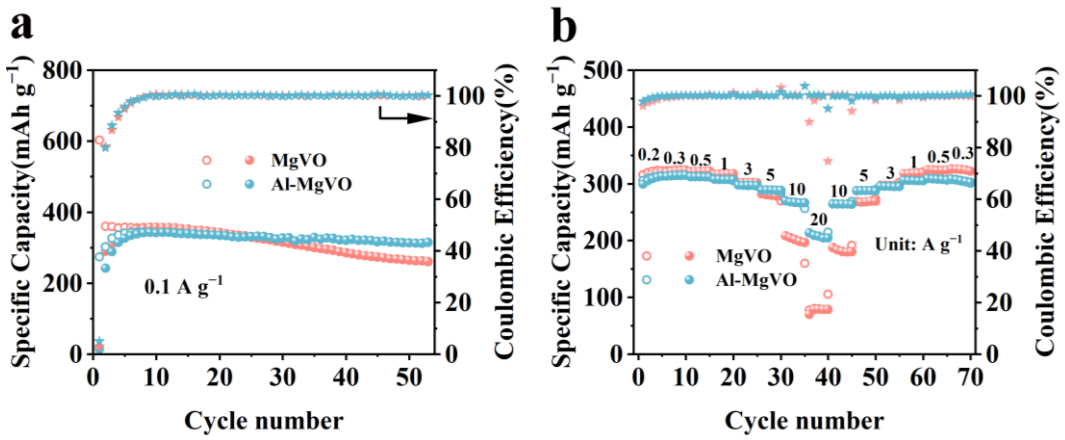

Figure 5. (**a**) Cycling performance of MgVO and Al-MgVO at 0.1 A g^{-1}; (**b**) Rate performance of MgVO and Al-MgVO at different current densities.

Figure 5b presents the rate capability of MgVO and Al-MgVO at various current densities. At current densities of 0.2, 0.3, 0.5, 1, 3, 5, 10, and 20 A g^{-1}, Al-MgVO delivered specific capacities of 313.4, 315.2, 312.3, 307.2, 297, 288.7, 266.2, and 207.9 mAh g^{-1}, respectively. When the current density was reduced from 20 A g^{-1} to 10, 5, 3, 1, 0.5, and 0.3 A g^{-1}, the capacity recovered to 308.4 mAh g^{-1}, indicating excellent structural stability and tolerance to the fast insertion and extraction of Zn^{2+} ions. The outstanding rate capability of Al-MgVO further underscores its superior electrochemical performance in high-rate conditions. In comparison, MgVO also exhibited good rate performance, but Al-MgVO demonstrated enhanced stability and higher specific capacity at higher current densities.

Then the cycling stability of Al-MgVO was systematically evaluated at high current densities of 10 A g^{-1} and 20 A g^{-1}, as shown in Figure 6a and 6b, respectively. These evaluations are crucial for assessing the material's practical applicability in AZIBs. At a current density of 10 A g^{-1}, Al-MgVO exhibited an initial discharge capacity of 11.4 mAh g^{-1}, and an initial charge capacity of 36 mAh g^{-1}. Interestingly, during subsequent cycles, the discharge and charge capacities increased sharply, reaching 271.6 mAh g^{-1}, and the Coulombic efficiency (CE) gradually approached 100%. This remarkable capacity enhancement can be attributed to the gradual activation of the electrode material, which is mainly driven by an irreversible phase transition in the electrode. This phase transition led

 doi:10.20944/preprints202503.2266.v1

to an increase in the oxidation state of vanadium (V), which subsequently facilitated the higher electrochemical performance of Al-MgVO. After 1000 cycles, the material retained a capacity of 254.3 mAh g^{-1}, corresponding to a high capacity retention of 93.6%. This excellent cycling performance demonstrates the material's potential for high-rate cycling stability and is a clear indication of the favorable influence of aluminum ions in stabilizing the MgVO structure.

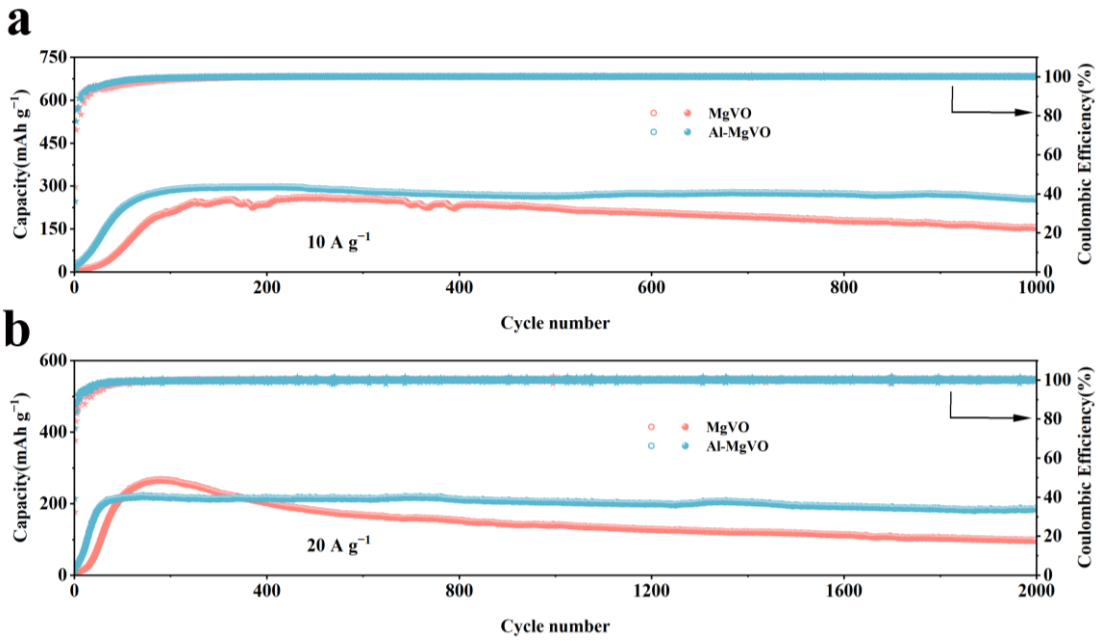

Figure 6. Long-cycle stability of MgVO and Al-MgVO at varying current densities: (a) 10 A g^{-1}; (b) 20 A g^{-1}.

Comparatively, the MgVO electrode, after activation, exhibited a relatively higher capacity but suffered from poorer cycling stability, with a faster capacity decay. This suggests that the introduction of Al^{3+} ions into the MgVO structure plays a significant role in enhancing the electrochemical performance and long-term stability of Al-MgVO. The Al^{3+} ions act as a structural pillar, forming stable Al–O bonds with oxygen atoms, thus reinforcing the crystal lattice and preventing structural collapse during cycling. Moreover, aluminum ions do not occupy excessive Zn^{2+} storage sites, which optimizes the electronic structure of MgVO and reduces the interaction between Zn^{2+} and the host material, resulting in more efficient cycling behavior at higher current densities.

At an even higher current density of 20 A g^{-1}, Al-MgVO demonstrated an initial discharge capacity of 11.6 mAh g^{-1} and an initial charge capacity of 12.4 mAh g^{-1}. After 70 cycles, the discharge and charge capacities significantly improved, reaching 207 mAh g^{-1}, with the Coulombic efficiency maintaining a near-perfect value of 100%. After 2000 cycles, the material exhibited a capacity of 186.8 mAh g^{-1}, yielding a capacity retention of 90.2%. The sustained high Coulombic efficiency and capacity retention underline the robustness of Al-MgVO under ultra-high current conditions, reinforcing its suitability as a promising cathode material for AZIBs.

The superior cycling stability and high capacity of Al-MgVO at both 10 A g^{-1} and 20 A g^{-1} can be attributed to the structural modifications induced by the incorporation of Al^{3+} ions. These ions not only enhance the structural integrity of the material but also optimize its electrochemical performance by minimizing detrimental side reactions and reducing the impact of Zn^{2+} ion interactions. Furthermore, the ability of Al-MgVO to maintain high Coulombic efficiency and stable capacity over long cycling periods at these elevated current densities is a testament to its potential for high-rate, long-life applications in energy storage technologies.

To further investigate the outstanding cycling stability and rate performance of Al-MgVO as a cathode material for zinc-ion batteries, CV tests were conducted at various scan rates ranging from

 doi:10.20944/preprints202503.2266.v1

0.1 to 1 mV s^{-1}. The CV curves obtained at different scan rates, as shown in Figure 7a, provide valuable insights into the electrochemical behavior of Al-MgVO.

At lower scan rates (0.1 and 0.2 mV s^{-1}), the CV curves exhibit well-defined oxidation and reduction peaks, characteristic of the reversible intercalation and de-intercalation of zinc ions. As the scan rate increases, the oxidation peak is observed to shift slightly toward higher potentials, while the reduction peak moves towards lower potentials. This shift can be attributed to the increased influence of kinetic factors at higher scan rates, where the ion diffusion process becomes less efficient. Despite this shift, the overall shape of the CV curves remains well-preserved across all scan rates, which suggests that Al-MgVO maintains its electrochemical reversibility and structural integrity even at higher scan rates. Notably, at the highest scan rate (1 mV s^{-1}), the CV curve retains its characteristic shape. This indicates that Al-MgVO is capable of undergoing fast redox reactions while preserving its electrochemical performance. The consistency of the CV profiles at higher scan rates signifies that Al-MgVO can effectively accommodate rapid ion insertion and extraction processes, which is crucial for high-rate performance in energy storage applications.

The observed behavior also implies that Al-MgVO serves as a robust host material that can withstand high discharge rates without significant degradation in performance. The electrochemical stability of Al-MgVO at varying scan rates highlights its potential for fast charge/discharge processes, which is desirable for applications that require both high capacity and high power density. In addition, the results suggest that the insertion of Al^{3+} ions into the MgVO structure enhances the material's structural stability, allowing it to better endure the stresses induced during rapid cycling. This structural robustness under high scan rates is likely one of the key factors contributing to the superior cycling stability and rate capability of Al-MgVO.

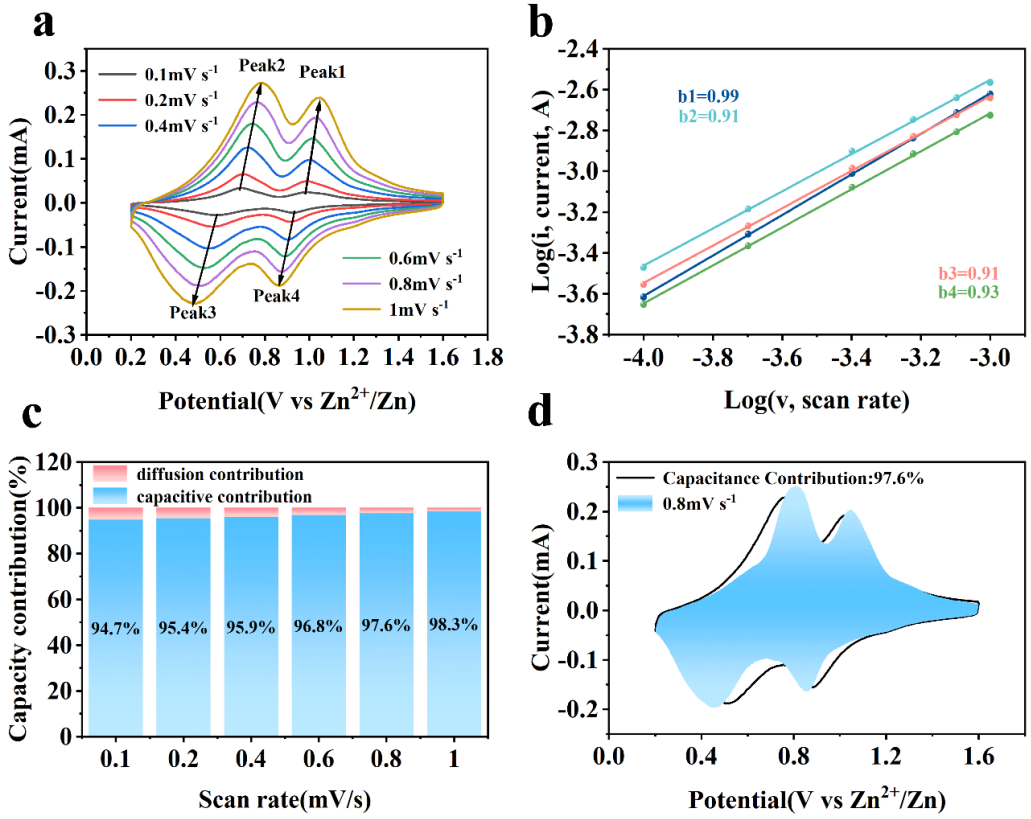

Figure 7. (**a**) CV of Al-MgVO at different sweep speeds; (**b**) *b*-value; (**c**) pseudocapacitance contribution at different scan rates; (**d**) pseudocapacitance contribution at 0.8 mV s^{-1}.

To elucidate the contribution of pseudocapacitance in Al-MgVO, the relationship between peak current (i) and scan rate (v) was explored through the empirical formula $i = av^b$, where a and b are adjustable parameters. Typically, the exponent b ranges between 0.5 and 1, serving as an indicator of

 doi:10.20944/preprints202503.2266.v1

the underlying charge storage mechanism—diffusion-controlled or capacitive-controlled processes. Commonly, a *b* value close to 1 is indicative of capacitive behavior, while a value around 0.5 suggests diffusion control.

In the studied case of Al-MgVO, the *b* values corresponding to the four redox peaks (Peak1, Peak2, Peak3, Peak4) at various scan rates (0.1, 0.2, 0.4, 0.6, 0.8, and 1 mV s^{-1}) were found to be 0.99, 0.91, 0.91, and 0.93, respectively. These values suggest that capacitive behavior predominates in the charge storage process. This is further evidenced by the near unity *b* values particularly at Peak1, indicating that the redox reactions within the Al-MgVO are primarily governed by the rate of the electrochemical reactions rather than by ionic diffusion.

This dominant capacitive behavior implies that the charge storage mechanism in Al-MgVO is significantly influenced by surface or near-surface electrochemical processes, rather than the bulk diffusion of ions into the electrode material. Such characteristics are beneficial for high power applications where rapid charge and discharge cycles are crucial. Additionally, the capacitive control of the redox reactions hints at the possibility of engineering the electrode's surface properties to enhance this behavior, potentially leading to improved cycle stability and rate capability in AZIBs. Moreover, the consistency of the *b* values across different scan rates underscores the robustness of the pseudocapacitive contribution.

To further quantitatively analyze the pseudocapacitive contribution, it is essential to differentiate between capacitive control and diffusion processes, which can be determined based on current contributions. The current can be expressed as follows:

$$i = k_1 v + k_2 v^{1/2} \quad (1)$$

where i represents the current, $k_1 v$ corresponds to the capacitive-controlled contribution, and $k_2 v^{1/2}$ represents the diffusion-controlled contribution. By calculating the current responses at different voltages and scan rates, the capacitive and ion diffusion contributions can be separated, offering a deeper understanding of the electrochemical behavior.

The pseudocapacitive contribution of Al-MgVO at various scan rates is illustrated in Figure 7c. As the scan rate increases from 0.1 mV/s to 1.0 mV/s, the pseudocapacitive contribution steadily increases, reaching values of 94.7%, 95.4%, 95.9%, 96.8%, 97.6%, and 98.3%, respectively. This significant increase in pseudocapacitive contribution with higher scan rates is indicative of a dominant pseudocapacitive behavior at faster charge/discharge rates. Particularly, at a scan rate of 0.8 mV/s, the pseudocapacitive contribution reaches as high as 97.6% (Figure 7d), signifying that the electrochemical behavior of the Al-MgVO material is primarily governed by pseudocapacitive effects. The dominance of pseudocapacitance suggests high surface reactivity, which is favorable for achieving superior rate capability. High pseudocapacitive contributions are also indicative of an enhanced performance at high current densities and improved cycle stability, as observed in the long-cycle and rate capability tests.

The reaction kinetics of the Al-MgVO cathode material were investigated using the Galvanostatic Intermittent Titration Technique (GITT). GITT is a technique for evaluating the relationship between diffusion coefficients and charge transfer in electrochemical systems, as described by the following equation:

$$D^{GITT} = \frac{4}{\pi\tau}\left(\frac{m_s V_M}{M_s S}\right)^2 \left(\frac{\Delta E_s}{\Delta E_t}\right)^2 \quad (2)$$

where D^{GITT} is the diffusion coefficient, τ is the time of the current pulse, m_s is the mass of the electrode, V_M is the molar volume of the active material, M_s is the molar mass of the active material, S is the surface area of the electrode, ΔE_s is the steady-state potential change, and ΔE_t is the potential change at the beginning of the current pulse.

As shown in Figure 8, the diffusion coefficient of Al-MgVO is observed to be in the range of 10^{-9} to 10^{-10} cm^2 s^{-1}. In contrast, the diffusion coefficient of Zn^{2+} in the MgVO material is in the range of 10^{-11} to 10^{-12} cm^2 s^{-1}. This significant difference can be attributed to the Al doping, which increases the

 doi:10.20944/preprints202503.2266.v1

electronegativity of the material and enhances its adsorption ability. This, in turn, facilitates a faster charge transfer rate, leading to an accelerated diffusion of Zn^{2+} within the Al-MgVO structure. The increased diffusion rate of Zn^{2+} in Al-MgVO suggests that Al doping not only improves the electrochemical performance by enhancing ion diffusion but also contributes to the material's superior rate capability. These results provide a clear indication that Al-MgVO exhibits better electrochemical kinetics compared to its MgVO counterpart, which is advantageous for high-performance AZIBs.

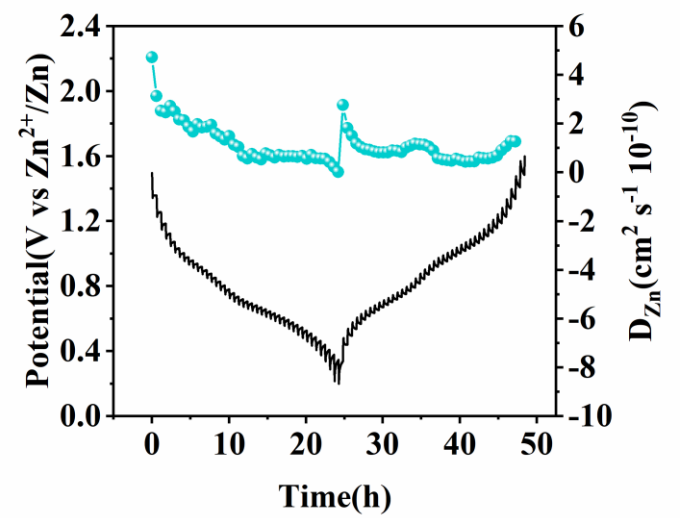

Figure 8. GITT curves and diffusion coefficients of Zn^{2+} for Al-MgVO at 0.1 A g^{-1}.

To further investigate the influence of Al doping on the conductivity of the MgVO material, EIS was employed to evaluate the charge transfer resistance and ion diffusion resistance of both Al-MgVO and MgVO before and after cycling. The high-frequency region of the EIS spectrum, represented by the semicircular arc, reflects the charge transfer resistance, while the low-frequency region corresponds to the linear section, which represents the ion diffusion resistance.

The EIS spectra of Al-MgVO and MgVO before cycling are shown in Figure 9a. It can be observed that the charge transfer resistance of Al-MgVO is significantly lower than that of MgVO, suggesting that the insertion of Al^{3+} ions has effectively reduced the resistance of MgVO. Lower charge transfer resistance is favorable for the migration of Zn^{2+} ions, leading to improved rate performance and enhanced cycling stability at high current densities in Al-MgVO. This improvement can be attributed to the incorporation of Al^{3+} ions, which optimize the electronic structure of the material. Furthermore, the formation of stable Al–O bonds between Al and oxygen results in a substantial reduction of the electrostatic interaction between Zn^{2+} ions and the host material, thereby enhancing the conductivity of MgVO and promoting its electrochemical performance.

 doi:10.20944/preprints202503.2266.v1

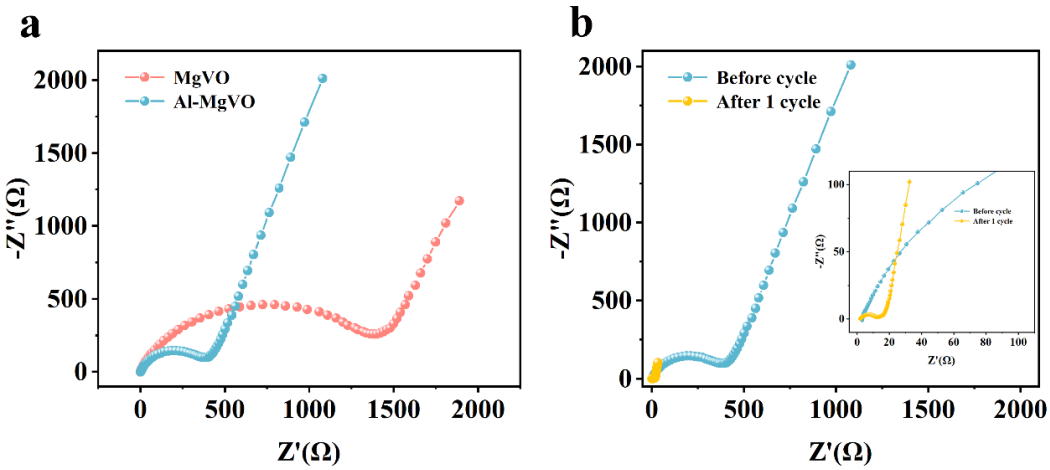

Figure 9. (**a**) Impedance spectra of MgVO and Al-MgVO; (**b**) Impedance spectra before and after cycling of Al-MgVO.

In addition, the EIS analysis after one cycle was conducted to further investigate the change in charge transfer resistance post-cycling (Figure 9b). The results indicate that the charge transfer resistance of Al-MgVO after one cycle is much lower compared to the pre-cycling resistance. This provides further confirmation that, although the initial capacity is relatively low, the specific capacity of Al-MgVO increases dramatically after one cycle. This phenomenon can be attributed to the self-optimization of the electrode during the first cycle, which effectively enhances the conductivity of the material. The improvement in conductivity during the activation process leads to a significant enhancement of the electrochemical performance, making the Al-MgVO electrode more efficient in subsequent cycles.

3. Materials and Methods

3.1. Preparation of Material

The spinel MgVO was synthesized using the sol-gel method as follows: 2 mmol of magnesium acetate tetrahydrate and 4 mmol of vanadium acetylacetonate were dissolved in 200 ml of anhydrous ethanol and subjected to ultrasonic treatment for 30 minutes. The resulting solution was then stirred at room temperature at 600 rpm for 3 hours. Subsequently, the mixture was placed in a water bath, and the solvent was evaporated at 80°C to yield the MgVO precursor. The obtained solid was dried in an electric drying oven at 60°C for 12 hours, followed by grinding into a fine powder. Finally, the powder was calcined in an argon atmosphere at 800°C for 12 hours with a heating rate of 2°C/min to obtain the MgVO product.

To synthesize Al-MgVO, 0.5 mmol of aluminum nitrate nonahydrate, 2 mmol of magnesium acetate tetrahydrate, and 4 mmol of vanadium acetylacetonate were dissolved in 200 ml of anhydrous ethanol. The synthesis procedure was then carried out as described for the preparation of MgVO, resulting in the formation of Al-MgVO.

3.2. Materials Characterization

The XRD measurements were conducted using Cu Kα radiation with a Smart Lab SE system (Tokyo, Japan), providing detailed insights into the crystalline structure of the materials. Morphological analyses were performed using scanning electron microscopy (SEM) to examine the surface features of the materials. SEM images were obtained with a Hitachi SU8010 microscope (Tokyo, Japan), enabling high-resolution visualization of the material surfaces.

The elemental distribution within the synthesized materials was evaluated using EDS integrated into the SEM system. This technique facilitated qualitative analysis of the elemental composition at various points across the samples, offering insights into the uniformity and purity of the materials.

 doi:10.20944/preprints202503.2266.v1

Additionally, the elemental composition was determined quantitatively using an ICP optical emission spectrometer (ICP-OES, Optima 8000, MA, USA).

The XPS was further employed to investigate the elemental composition and to monitor changes in the oxidation states of the constituent elements. These analyses were carried out using a Thermo ESCALAB 250Xi spectrometer (Waltham, MA, USA), which provided high-resolution spectral data for both powder samples and sliced electrode materials. This technique was particularly useful for understanding the electronic environment of the elements and tracking changes associated with electrochemical processes.

3.3. Electrode Fabrication

The cathode material (MgVO), conductive agent (acetylene black), and binder (polyvinylidene fluoride, PVDF) were mixed in a mass ratio of 6:3:1 and placed into a mortar for uniform blending. The mixture was ground continuously until a homogeneous consistency was achieved, at which point N-methylpyrrolidone (NMP) was incrementally added to form a uniform slurry. The slurry was kneaded continuously until a glossy appearance was observed. Subsequently, the slurry was coated onto titanium foil (thickness: 0.03 mm) and vacuum-dried at 110°C for 12 hours. After drying, the titanium foil was punched into electrode discs with a diameter of 10 mm, achieving an active material loading of approximately 1–1.6 mg cm^{-2}.

For the coin cell assembly, zinc foil (0.1 mm) was employed as the anode, and 3M $Zn(CF_3SO_3)_2$ solution was used as the electrolyte. A glass fiber separator was incorporated, with titanium foil serving as the current collector. The synthesized cathode material was utilized as the positive electrode. The coin cell was assembled under ambient air conditions at room temperature, followed by sealing using a sealing machine.

3.4. Electrochemical Measurements

The CV analyses were performed using a coin cell configuration on a CHI 760E electrochemical workstation. The cathode sheet, coated with the active material, served as the working electrode and was evaluated within a voltage range of 0.2 V to 1.6 V (vs. Zn/Zn^{2+}) at scan rates of 0.1, 0.2, 0.4, 0.6, 0.8, and 1 mV s^{-1}. The EIS measurements were conducted by applying a small-amplitude sinusoidal AC signal, enabling the assessment of the system's impedance. The acquired data were analyzed using equivalent circuit modeling on the CHI 760E, with a frequency range from 0.01 Hz to 100 kHz and a voltage amplitude of 5 mV. The GITT was utilized to investigate the diffusion processes and the interaction between charge transfer and electrochemical reactions at the electrode surface. This method involved cycles of pulse application, constant current, and relaxation, which allowed for the determination of the chemical diffusion coefficient. These tests were conducted using the CT2001A Battery Test System (Wuhan LAND Electric Co.). Furthermore, electrochemical cycling and rate capability tests were carried out at room temperature on coin cells at varying current densities ranging from 0.1 to 20.0 A g^{-1}, employing the same CT2001A system. Collectively, these methodologies facilitated a comprehensive evaluation of the electrochemical properties of the examined electrodes.

4. Conclusions

In conclusion, this study highlights the successful development of Al-doped MgVO spinel cathodes for AZIBs, addressing key challenges such as poor ion diffusion and structural instability. By pre-inserting Al^{3+} ions into the spinel structure via a sol-gel method, the Al-doped MgVO cathode demonstrates significant improvements in both structural stability and electronic conductivity. The Al^{3+} ions form strong Al–O bonds, which reduce the electrostatic interactions between Zn^{2+} ions and the host material, thereby facilitating more efficient Zn^{2+} intercalation and deintercalation.

The Al-MgVO cathode exhibits excellent electrochemical performance, particularly at high current densities. At 10 A g^{-1}, the material maintains a capacity of 254.3 mAh g^{-1} after 1000 cycles,

 doi:10.20944/preprints202503.2266.v1

with a remarkable capacity retention of 93.6%. More importantly, at an ultra-high current density of 20 A g^{-1}, it retains a capacity of 186.8 mAh g^{-1} after 2000 cycles, with a capacity retention of 90.2%, making it an outstanding candidate for high-rate applications in large-scale energy storage systems. These results suggest that Al-doped MgVO cathodes offer a promising solution for enhancing the performance of AZIBs, demonstrating the potential for sustainable, high-rate energy storage. Further optimization of this material could lead to significant improvements in the performance and viability of AZIBs for large-scale applications.

Author Contributions: Conceptualization, H.L. and Z.W.; methodology, H.L. and Y.Z.; software, Y.Z.; validation, H.L., Z.W. and Y.Z.; formal analysis, H.L. and Z.W.; investigation, H.L., Z.W. and Y.Z.; resources, Z.W.; data curation, Y.Z.; writing—original draft preparation, H.L.; writing—review and editing, H.L., Z.W. and Y.Z.; visualization, Z.W. and Y.Z.; supervision, H.L.; project administration, H.L.; funding acquisition, H.L. All authors have read and agreed to the published version of the manuscript.

Funding: This research was funded by the National Natural Science Foundation of China, grant number 22065032, and the Graduate Education and Teaching Research and Reform Project of Universities in Xinjiang Autonomous Region, grant number XJGXPTJG-202205. The APC was funded by High Level Overseas Educated Talents Returning to China Funding Candidate Program, grant number 2019160.

Data Availability Statement: The data presented in this study are available on request from the corresponding author.

Acknowledgments: The authors acknowledge the Shiyanjia Lab (www.shiyanjia.com accessed on 5 March 2025) for the SEM tests.

Conflicts of Interest: The authors declare no conflicts of interest.

References

1. Algarni, S.; Tirth, V.; Alqahtani, T.; Alshehery, S.; Kshirsagar, P. Contribution of renewable energy sources to the environmental impacts and economic benefits for sustainable development. *Sustain. Energy. Techn.* **2023**, *56*, 103098.
2. Wan, F.; Niu, Z. Design strategies for vanadium-based aqueous zinc-ion batteries. *Angew. Chem. Int. Edit.* **2019**, *131*, 16508–16517.
3. Chen, S.P.; Lv, D.; Chen, J.; Zhang, Y.H.; Shi, F.N. Review on defects and modification methods of $LiFePO_4$ cathode material for lithium-ion batteries. *Energy Fuels* **2022**, *36*, 1232–1251.
4. Blanc, L.E.; Kundu, D.; Nazar, L.F. Scientific challenges for the implementation of Zn-ion batteries. *Joule* **2020**, *4*, 771–799.
5. Li, G.; Sun, L.; Zhang, S.; Zhang, C.; Jin, H.; Davey, K.; Liang, G.; Liu, S.; Mao, J.; Guo, Z. Developing cathode materials for aqueous zinc ion batteries: challenges and practical prospects. *Adv. Funct. Mater.* **2024**, *34*, 2301291.
6. Chen, S.P.; Lv, D.; Chen, J.; Zhang, Y.H.; Shi, F.N. Review on defects and modification methods of $LiFePO_4$ cathode material for lithium-ion batteries. *Energy Fuels* **2022**, *36*, 1232–1251.
7. Jin, Y.; Zhang, T.; Zhang, M. Advances in intelligent regeneration of cathode materials for sustainable lithium-ion batteries. *Adv. Energy Mater.* **2022**, *12*, 2201526.
8. Xu, J.; Cai, X.; Cai, S.; Shao, Y.; Hu, C.; Lu, S.; Ding, S. High-energy lithium-ion batteries: recent progress and a promising future in applications. *Energy Environ. Mater.* **2023**, *6*, e12450.
9. Wei, M.; Zhang, Y.; Gu, Y.; Wang, Z.; Ye, H.; Wang, Y.; Qu, S.; Hu, K.; Zhao, J.; Liu, C.; Jia, D.; Lin, H. Experimental validation of density functional theory predictions on structural water impact in vanadium oxide cathodes for zinc-ion batteries. *Small* **2024**, *20*, 2406801.
10. Hu, J.; Xu, L.; Li, X.; Liang, Q.; Ding, C.; Li, Y.; Liu, Y.; Gao, Y. Pre-sodiation strategies for constructing high-performance sodium-ion batteries. *J. Mater. Chem. A* **2025**, *13*, 3206–3235.
11. Zhang, Z.; Wang, X.; Zhu, J.; Li, N.; Wang, L.; Yang, Y.; Chen, Y.; Tan, L.; Niu, X.; Wang, X.; Li, X.; Zhu, Y. Electrolyte design enables stable and energy-dense potassium-ion batteries. *Angew. Chem. Int. Edit.* **2025**, *64*, e202415491.
12. Fu, Z.; Zhang, H.; Geng, D.; Liu, Z.; Zhang, Z.; Li, X.; Yan, C. Constructing sulfur-heterocyclic aromatic amine polymer with multiple-redox active sites for long-lifespan and all-organic aqueous magnesium ion batteries. *Adv. Energy Mater.* **2025**, *15*, 2403934.
13. Wang, M.; Meng, Y.; Li, X.; Qi, J.; Li, A.; Huang, S. Challenges and strategies for zinc anodes in aqueous Zinc-Ion batteries. *Chem. Eng. J.* **2025**, *507*, 160615.
14. Lv, T.; Zhu, G.; Dong, S.; Kong, Q.; Peng, Y.; Jiang, S.; Zhang, G.; Yang, Z.; Yang, S.; Dong, X.; Pang, H.; Zhang, Y. Co-intercalation of dual charge carriers in metal-ion-confining layered vanadium oxide nanobelts for aqueous zinc-ion batteries. *Angew. Chem. Int. Edit.* **2023**, *135*, e202216089.

 doi:10.20944/preprints202503.2266.v1

15. Li, J.; Wang, C.; Yu, Z.; Chen, Y.; Wei, L. MXenes for zinc-based electrochemical energy storage devices. *Small* **2024**, *20*, 2304543.
16. Zhang, L.; Hu, J.; Zhang, B.; Liu, J.; Wan, H.; Miao, L.; Jiang, J. Suppressing cathode dissolution via guest engineering for durable aqueous zinc-ion batteries. *J. Mater. Chem. A* **2021**, *9*, 7631–7639.
17. Yi, Z.; Chen, G.; Hou, F.; Wang, L.; Liang, J. Strategies for the stabilization of Zn metal anodes for Zn-ion batteries. *Adv. Energy Mater.* **2021**, *11*, 2003065.
18. Zhu, J.; Tie, Z.; Bi, S.; Niu, Z. Towards more sustainable aqueous zinc-ion Batteries. *Angew. Chem. Int. Edit.* **2024**, *136*, e202403712.
19. Lv, T.; Peng, Y.; Zhang, G.; Jiang, S.; Yang, Z.; Yang, S.; Pang, H. How about vanadium-based compounds as cathode materials for aqueous zinc ion batteries? *Adv. Sci.* **2023**, *10*, 2206907.
20. Guo, C.; Yi, S.; Si, R.; Xi, B.; An, X.; Liu, J.; Li, J.; Xiong, S. Advances on defect engineering of vanadium-based compounds for high-energy aqueous zinc-ion batteries. *Adv. Energy Mater.* **2022**, *12*, 2202039.
21. Ding, Y.; Zhang, L.; Wang, X.; Han, L.; Zhang, W.; Guo, C. Vanadium-based cathodes for aqueous zinc ion batteries: structure, mechanism and prospects. *Chin. Chem. Lett.* **2023**, *34*, 107399.
22. Zhang, N.; Wang, J.-C.; Guo, Y.-F.; Wang, P.-F.; Zhu, Y.-R.; Yi, T.-F. Insights on rational design and energy storage mechanism of Mn-based cathode materials towards high performance aqueous zinc-ion batteries. *Coord. Chem. Rev.* **2023**, *479*, 215009.
23. Chen, D.; Lu, M.; Cai, D.; Yang, H.; Han, W. Recent advances in energy storage mechanism of aqueous zinc-ion batteries. *J. Energy Chem.* **2021**, *54*, 712–726.
24. Wang, X.; Zhang, Z.; Xi, B.; Chen, W.; Jia, Y.; Feng, J.; Xiong, S. Advances and perspectives of cathode storage chemistry in aqueous zinc-ion batteries. *ACS Nano* **2021**, *15*, 9244–9272.
25. Yi, T.; Qiu, L.; Qu, J.; Liu, H.; Zhang, J.; Zhu, Y. Towards high-performance cathodes: Design and energy storage mechanism of vanadium oxides-based materials for aqueous Zn-ion batteries. *Coord. Chem. Rev.* **2021**, *446*, 214124.
26. Liu, Y.; Zhang, J.; Liu, Y.; Zhang, M.; Pan, Z.; Cai, K. Controllable design of metal-organic framework-derived vanadium oxynitride for high-capacity and long-cycle aqueous Zn-ion batteries. *Small* **2024**, *20*, 2401922.
27. Chen, D.; Lu, M.; Wang, B.; Cheng, H.; Yang, H.; Cai, D.; Han, W.; Fan, H.J. High-mass loading $V_3O_7 \cdot H_2O$ nanoarray for Zn-ion battery: New synthesis and two-stage ion intercalation chemistry. *Nano Energy* **2021**, *83*, 105835.
28. Zhang, N.; Jia, M.; Dong, Y.; Wang, Y.; Xu, J.; Liu, Y.; Jiao, L.; Cheng, F. Hydrated layered vanadium oxide as a highly reversible cathode for rechargeable aqueous zinc batteries. *Adv. Funct. Mater.* **2019**, *29*, 1807331.
29. Yang, Y.; Zhou, J.; Wang, L.; Jiao, Z.; Xiao, M.; Huang, Q.; Liu, M.; Shao, Q.; Sun, X.; Zhang, J. Prussian blue and its analogues as cathode materials for Na-, K-, Mg-, Ca-, Zn- and Al-ion batteries. *Nano Energy* **2022**, *99*, 107424.
30. Zeng, Y.; Lu, X.F.; Zhang, S.L.; Luan, D.; Li, S.; Lou, X.W. Construction of Co–Mn prussian blue analog hollow spheres for efficient aqueous Zn-ion batteries. *Angew. Chem. Int. Edit.* **2021**, *60*, 22189–22194.
31. Zhou, T.; Zhu, L.; Xie, L.; Han, Q.; Yang, X.; Chen, L.; Wang, G.; Cao, X. Cathode materials for aqueous zinc-ion batteries: A mini review. *J. Colloid. Interf. Sci.* **2022**, *605*, 828–850.
32. Zhao, D.; Li, Z.; Xu, D.; Yang, Z. Multiple redox-active cyano-substituted organic compound integrated with MXene nanosheets for high-performance flexible aqueous Zn-ion battery. *Adv. Funct. Mater.* **2024**, *34*, 2316182.
33. Zhang, Y.; Li, Y.; Yao, S.; Ali, N.; Kong, X.; Wang, J. High-performance organic electrodes for sustainable zinc-ion batteries: Advances, challenges and perspectives. *Energy Storage Mater.* **2024**, *71*, 103544.
34. Liu, Y.; Lu C.; Yang, Y.; Chen, W.; Ye, F.; Dong, H.; Wu, Y.; Ma, R.; Hu, L. Multiple cations nanoconfinement in ultrathin V_2O_5 nanosheets enables ultrafast Ion diffusion kinetics toward high-performance zinc ion battery. *Adv. Mater.* **2024**, *36*, 2312982.
35. Guo, C.; Yi, S.; Si, R.; Xi, B.; An, X.; Liu, J.; Li, J.; Xiong, S. Toward low-temperature zinc-ion batteries: strategy, progress, and prospect in vanadium-based cathodes. *Adv. Energy Mater.* **2024**, *14*, 2304010.
36. Song, Z.; Zhao, Y.; Zhou, A.; Wang, H.; Jin, X.; Huang, Y.; Li, L.; Wu, F.; Chen, R. Organic intercalation induced kinetic enhancement of vanadium oxide cathodes for ultrahigh-loading aqueous zinc-ion batteries. *Small* **2024**, *20*, 2305030.
37. Zhou, J.; Shan, L.; Wu, Z.; Guo, X.; Fang, G.; Liang, S. Investigation of V_2O_5 as a low-cost rechargeable aqueous zinc ion battery cathode. *Chem. Commun.* **2018**, *54*, 4457–4460.
38. Hu, H.; Zhao, P.; Li, X.; Liu, J.; Liu, H.; Sun, B.; Pan, K.; Song, K.; Cheng, H. Heterojunction tunnelled vanadium-based cathode materials for high-performance aqueous zinc ion batteries. *J. Colloid Interface Sci.* **2024**, *665*, 564–572.
39. Chen, X.; Zhang, H.; Liu, J.-H.; Gao, Y.; Cao, X.; Zhan, C.; Wang, Y.; Wang, S.; Chou, S.-L.; Dou, S.-X.; Cao, D. Vanadium-based cathodes for aqueous zinc-ion batteries: mechanism, design strategies and challenges. *Energy Storage Mater.* **2022**, *50*, 21–46.
40. Lee, W.; Muhammad, S.; Sergey, C.; Lee, H.; Yoon, J.; Kang, Y.M.; Yoon, W.S. Advances in the cathode materials for lithium rechargeable batteries. *Angew. Chem. Int. Edit.* **2020**, *59*, 2578–2605.

 doi:10.20944/preprints202503.2266.v1

41. Mao, S.; Shen, Z.; Zhang, W.; Wu, Q.; Wang, Z.; Lu, Y. Outside-in nanostructure fabricated on $LiCoO_2$ surface for high-voltage lithium-ion batteries. *Adv. Sci.* **2022**, *9*, 2104841.
42. Zhang, X.D.; Shi, J.L.; Liang, J.Y.; Yin, Y.X.; Zhang, J.N.; Yu, X.Q.; Guo, Y.G. Suppressing surface lattice oxygen release of Li-rich cathode materials via heterostructured spinel $Li_4Mn_5O_{12}$ coating. *Adv. Mater.* **2018**, *30*, 1801751.
43. Yuan, J.; Qiao, Y.; Li, Y.; Xu, H.; Zhang, W.; Zhang, Z.; He, G.; Chen, H. Diminishing the migration resistance of zinc ions by cation vacancy engineering in a spinel-framework. *J. Mater. Chem. A* **2024**, *12*, 4877–4883.
44. Yan, L.; Xu, Z.; Hu, W.; Ning, J.; Zhong, Y.; Hu, Y. Formation of sandwiched leaf-like CNTs-Co/$ZnCo_2O_4$@NC-CNTs nanohybrids for high-power-density rechargeable Zn-air batteries. *Nano Energy* **2021**, *82*, 105710.
45. Soundarrajan, V.; Sambandam, B.; Kim, S.; Mathew, V.; Jo, J.; Kim, S.; Lee, J.; Islam, S.; Kim, K.; Sun, Y.K.; Kim, J. Aqueous magnesium zinc hybrid battery: an advanced high-voltage and high-energy $MgMn_2O_4$ cathode. *ACS Energy Lett.* **2018**, *3*, 1998–2004.
46. Tang, W.; Lan, B.; Tang, C.; An, Q.; Chen, L.; Zhang, W.; Zou, C.; Dong, S.; Luo, P. Urchin-like spinel MgV_2O_4 as a cathode material for aqueous zinc-ion batteries. *ACS Sustainable Chem. Eng.* **2020**, *8*, 3681–3688.
47. Feng, Z.; Zhang, Y.; Sun, J.; Liu, Y.; Jiang, H.; Cui, M.; Hu, T.; Meng, C. Dual ions enable vanadium oxide hydration with superior Zn^{2+} storage for aqueous zinc-ion batteries. *Chem. Eng. J.* **2022**, *433*, 133795.
48. Wang, X.; Wang, Y.; Naveed, A.; Li, G.; Zhang, H.; Zhou, Y.; Dou, A.; Su, M.; Liu, Y.; Guo, R.; Li, C.C. Magnesium ion doping and micro-structural engineering assist $NH_4V_4O_{10}$ as a high-performance aqueous zinc ion battery cathode. *Adv. Funct. Mater.* **2023**, *33*, 2306205.
49. Xing, L.; Zhang, C.; Li, M.; Hu, P.; Zhang, X.; Dai, Y.; Pan, X.; Sun, W.; Li, S.; Xue, J.; An, Q.; Mai, L. Revealing excess Al^{3+} preinsertion on altering diffusion paths of aluminum vanadate for zinc-ion batteries. *Energy Storage Mater.* **2022**, *52*, 291–298.